eScience 4 (2024) 100204

Contents lists available at ScienceDirect

eScience

journal homepage: www.keaipublishing.com/en/journals/escience

Research Paper

Unlocking power of neighboring vacancies in boosting hydrogen evolution reactions on two-dimensional $NiPS_3$ monolayer

Hyun Gu Han [a], Jae Won Choi [a], Minsu Son [b], Ki Chul Kim [a,b,*]

[a] Computational Materials Design Laboratory, Department of Chemical Engineering, Konkuk University, Seoul 05029, The Republic of Korea
[b] Division of Chemical Engineering, Konkuk University, Seoul 05029, The Republic of Korea

HIGHLIGHTS

- Defective engineering is adopted for design of high-performance $NiPS_3$ catalyst.
- Co-formation of vacancies in both Ni and S sites is the most effective approach.
- S-substitution-like physisorption of H_2O is observed on a vacant S site.
- The dissociative occupation of OH and H is observed for vacant sites of S and Ni.
- Origin of defect-dependent catalytic activity is unraveled by electronic analyses.

GRAPHICAL ABSTRACT

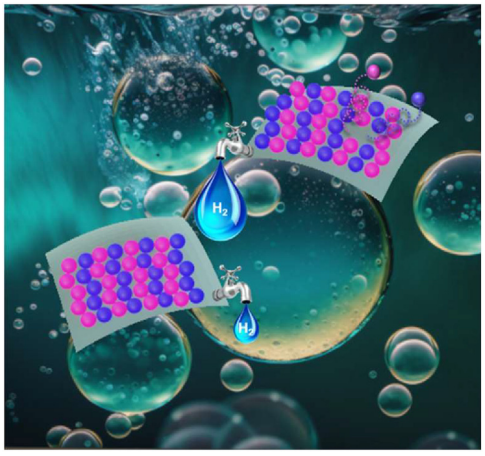

ARTICLE INFO

Keywords:
Hydrogen evolution reaction
Defect engineering
Transition metal phosphorus trichalcogenide
Density functional theory
Reaction thermodynamics

ABSTRACT

This study investigates the effect of defect engineering on the catalytic activity of a $NiPS_3$ monolayer catalyst for the hydrogen evolution reaction (HER). Three different types of vacancies on the basal plane of the monolayer are explored through a multi-step mechanism involving the dissociative adsorption of a water molecule and subsequent electrochemical adsorption of the dissociated proton. Co-formation of vacancies in both Ni and S sites is found to be the most effective in enhancing the catalytic performance of the monolayer. A key resource for the reaction thermodynamics is the S-substitution-like physisorption of a water molecule on a vacant S site, followed by the dissociative occupation of OH and H into vacant sites of S and Ni elements, boosted by the NiS di-vacancy configuration with low activation energy barriers. Investigation reveals the highest contribution of bonding orbitals to the monolayer-H bond makes it the most desirable defect engineering approach for transition metal phosphorus chalcogenides with high HER activities. Overall, this study highlights the significance of controlled defect engineering in augmenting the catalytic performance of $NiPS_3$ monolayer catalysts for HER.

* Corresponding author.
E-mail address: kich2018@konkuk.ac.kr (K.C. Kim).

https://doi.org/10.1016/j.esci.2023.100204
Received 28 April 2023; Received in revised form 15 September 2023; Accepted 11 October 2023
Available online 16 October 2023

1. Introduction

Hydrogen evolution reaction (HER) is a pivotal process in the field of renewable energy and electrochemistry, which refers to the release of hydrogen gas from a cathode in an electrochemical cell [1,2]. This reaction plays a critical role in the production of hydrogen fuel and the development of hydrogen-based energy storage systems. With increasing global interest in sustainable energy sources and a growing demand for clean energy technologies, the study of HER has gained significant attention in recent years. Furthermore, the challenge of achieving an efficient and cost-effective production of hydrogen through HER has been a prominent issue, especially in replacing Pt, the well-established best catalyst [3–5]. With the objective of overcoming this challenge, intensive efforts have been dedicated to developing two-dimensional catalysts (e.g., MoS_2 and VS_2) that can improve the efficiency and stability of the reaction [6–10]. For example, Ye *et al.* used a combined approach of oxygen plasma and hydrogen treatments to increase the surface density of catalytically active sites on MoS_2 monolayer and achieve a significant enhancement in its HER activity [6]. Meanwhile, Zhang *et al.* synthesized metallic VS_2 nanosheets with rich defects, using a facile one-pot solvothermal method [9]. They demonstrated that defect-rich environments and resultant modification in electronic structures could significantly enhance the electrocatalytic HER activity.

Recently, another two-dimensional structural family, transition metal phosphorus trichalcogenides (e.g., $MnPS_3$, $NiPS_3$, $MnPS_{1.5}Se_{1.5}$, and $NiPS_{1.5}Se_{1.5}$), have attracted special attention due to their intrinsic two-dimensional antiferromagnetism [11–14]. Among them, $NiPS_3$ is considered a promising candidate for HER electrocatalysis. Despite its potential, its unsatisfactory activity, originating from its semiconducting nature and the inertness of its basal plane, remains a challenge. Various experimental studies have been highlighted with an aim of activating catalytic activity of the basal plane [8,15,16]. For instance, Wang *et al.* doped the P site of a $NiPS_3$ monolayer with a non-metal heteroatom, such as B, C, N, or O, to activate its inert basal plane [15]. Zhang *et al.* have enhanced the catalytic activities for water splitting by decorating a pristine $NiPS_3$ monolayer with single-atom Co [16]. Although there have been notable developments in enhancing the structural activation of basal planes through defect engineering, there is still a need to further explore the chemistry underlying the defect-induced design of transition metal phosphorus trichalcogenides in order to identify an appropriate direction for design.

In conjunction with experimental efforts, the integration of computational protocols is crucial to the development of efficient and cost-effective catalysts for HER [3,4,17]. With the use of first-principles computational chemistry, researchers can gain a deeper understanding of the mechanisms and energetics of the reaction. This allows for predictions about the expected performance of carefully designed, unique catalysts without the need for extensive synthesis and testing. In addition, computational studies can provide a deeper understanding of the relationships between the structure of catalysts and their performance in HER, suggesting desired design directions and optimization of catalysts with specific properties and functions. In this study, the activation of the $NiPS_3$ monolayer surface is systematically designed through the induction of vacancies to gain insight into the fundamental chemistry underlying the impact of the vacancies on its catalytic activity. The first-principles density functional theory (DFT) calculations are employed to investigate the thermodynamics of vacancy formation as well as the correlations between the defect engineering and the catalytic performance of HER on the $NiPS_3$ monolayer. Our investigation reveals that the co-formation of vacancies in both Ni and S sites would be the most effective in enhancing the catalytic performance of the monolayer, particularly in the adsorptive dissociation of water molecules and the subsequent electrochemical adsorption of dissociated protons during multi-step HER mechanisms. Furthermore, the chemical origin of the vacancy-dependent performance difference is unraveled through electronic structure analyses.

2. Computational methods

General information on computational calculations: To model the bulk structure of two-dimensional layered $NiPS_3$, we used experimentally refined structural information (monoclinic structure with a symmetry of C2/m; lattice parameters: $a = 5.76$ Å, $b = 10.06$ Å, $c = 6.58$ Å, and $\beta = 107^\circ$) (Fig. 1) [18]. The geometrically optimized bulk unit cell exhibited lattice parameters of $a = 5.81$ Å, $b = 10.06$ Å, $c = 6.74$ Å and $\beta = 106.78^\circ$, which agree well with their experimental values, sustaining its experimental space group. Two-dimensional $NiPS_3$ monolayer models with two different slab sizes (i.e., (2×1) and (3×2) slab-like supercells) were then designed using the optimized bulk unit cell followed by atomic relaxation. To prevent unrealistic interactions between neighboring images, each monolayer model contained a vacuum of 20 Å along the z-direction. We also introduced either mono- or di-vacancy by removing Ni and/or S atoms from the monolayer models (Fig. 1). All bulk and slab calculations were performed using the Vienna *ab initio* simulation package with the projector augmented wave (PAW)[24] method with a cutoff energy of 400 eV. The generalized gradient approximation (GGA) parameterized by Perdew, Burke, and Ernzerhof (PBE) was applied with spin polarization [19–22]. During geometry optimization, all atoms were fully relaxed with an energy convergence tolerance of 10^{-5} eV per unit cell, and the final force on each atom was < 0.02 eV/Å. To better describe the highly localized *d* electrons, we employed the DFT + U approach in Dudarev's approximation with a Hubbard U correction ($U_{eff} = 4.0$ eV) to Ni for all DFT calculations [23,24]. Monkhorst-Pack grid points with $3 \times 3 \times 1$ and $1 \times 1 \times 1$ *k*-meshes were used for the atomic relaxation of (2×1) and (3×2) slab supercells, respectively, while deeper electronic analyses utilized $6 \times 6 \times 1$ *k*-meshes [25]. To account for the dispersion correction to potential energy, we used the zero damping DFT-D3 method for all calculations [26]. Additionally, we performed climbing image nudged elastic band (CI-NEB) calculations to obtain the potential energy surfaces along hydrogen evolution pathways [27]. Notably, $NiPS_3$ is more stable under an anti-ferromagnetic moment configuration than under a ferromagnetic one, thus the anti-ferromagnetic configuration was applied to all bulk and slab calculations [28,29].

HER thermodynamics: The Gibbs free energy change (ΔG_d) of water dissociation reaction on a catalyst surface can be defined as the following equations:

$$\Delta G_d = G_{*(H+OH)} - G_{*H_2O} \tag{1}$$

$$G = E + ZPE - TS \tag{2}$$

Here, $G_{*(H+OH)}$ and G_{*H_2O} represent the Gibbs free energies associated with the H–OH pair and H_2O adsorbed on the catalyst surface during the dissociative adsorption of a water molecule, respectively. The terms, *E*, *ZPE*, *S*, and *T* denote the DFT-calculated electronic energy, zero-point energy, entropy, and temperature (298.15 K in this study), respectively. Following a similar logic, the Gibbs free energy change (ΔG_{H^*} and ΔG_{OH^*}) associated with the electrochemical adsorption of a dissociated proton and hydroxyl ions on the catalyst surface can be calculated using the following equation.

$$\Delta G_{H^*} = G_{*H} - G_* - \frac{1}{2}G_{H_2} \tag{3}$$

$$\Delta G_{OH^*} = G_{*OH} - G_* - G_{H_2O} - \frac{1}{2}G_{H_2} \tag{4}$$

Here, G_*, G_{*H}, and G_{H_2} describe the Gibbs free energies associated with the catalyst surface, H adsorbed on the catalyst surface, and an isolated H_2 molecule, respectively. The theoretical exchange current density (i_0) can be calculated using Nørskov's assumption which states that the rate of the electrochemical reaction is proportional to the number of active sites on the catalyst surface and the probability of reaction per site. This can be expressed as [30]:

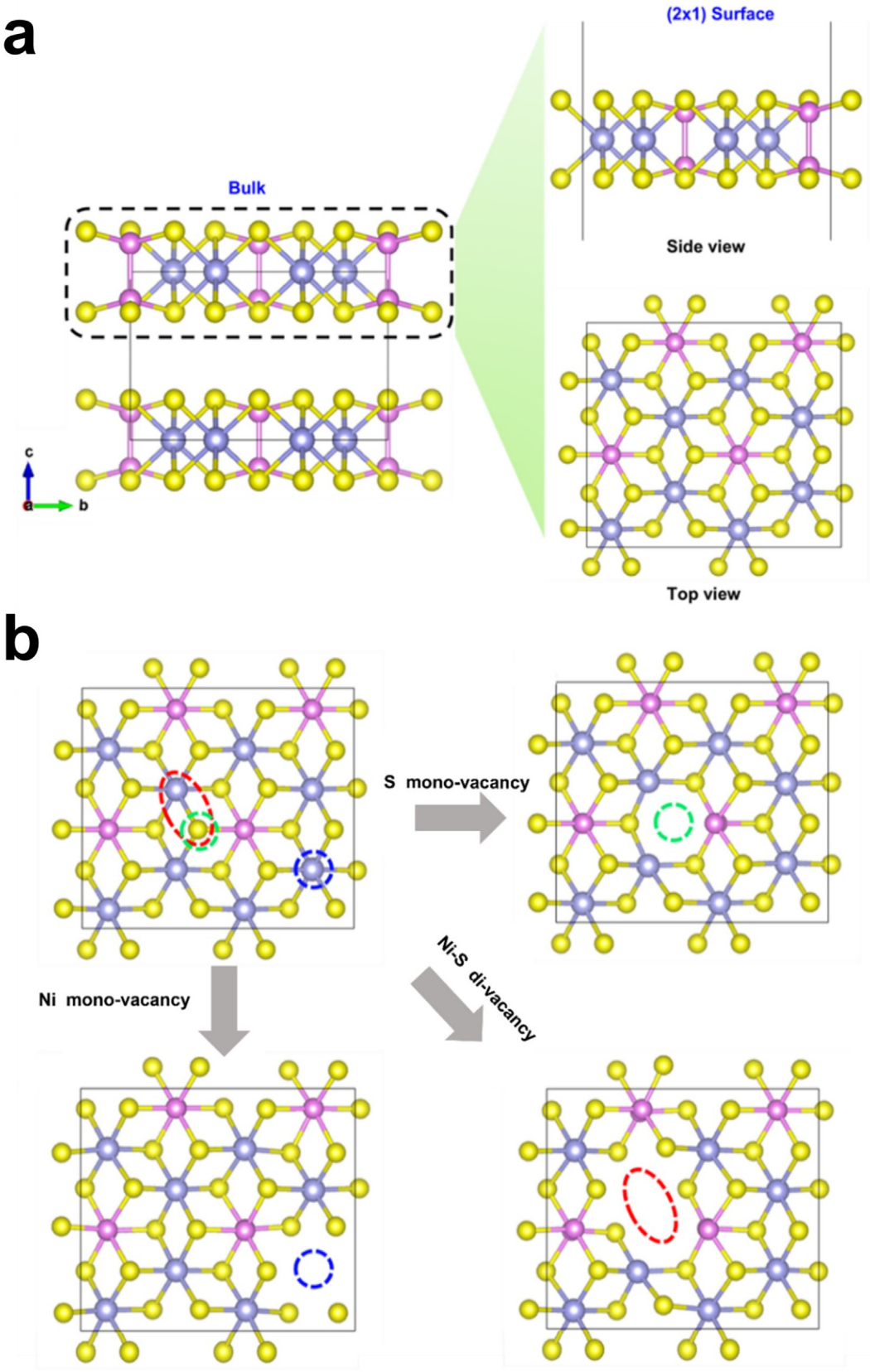

Fig. 1. (a) Bulk model of two-dimensional layered $NiPS_3$ structure and top/side views of its slab-like (2×1) monolayer supercell. (b) Pristine $NiPS_3$ monolayer model and its defective models with Ni-, S-, and Ni/S-vacancies. Atoms with blue, pink, and yellow in color depict nickel, phosphorus, and sulfur, respectively.

$$i_0 = -\frac{ek_0}{1+\exp\left(|\Delta G_{H^*}|/k_BT\right)} \tag{5}$$

Here k_0 is the rate constant that accounts for all factors related to solvent recombination observed during a proton transfer to the catalyst surface. In this study, we set k_0 to one for the sake of clarity in visualization.

Vacancy formation energy: The formation energy ($E^f[X]$) of a surface vacancy in a two-dimensional $NiPS_3$ monolayer model can be determined using the following equation [31]:

$$E^f[X] = E[X] - E[NiPS_3] - \sum_i n_i\mu_i \tag{6}$$

Here $E[X]$ and $E[NiPS_3]$ represent the DFT-calculated energies of $NiPS_3$ monolayer models with and without the neutral surface vacancies, respectively. Notably, defective sites on S and Ni elements are commonly observed for $NiPS_3$ catalysts [32]. Therefore, either S or Ni element was removed to create a mono-vacancy type, while the removal of a Ni–S element pair at their nearest neighboring positions was conducted for the di-vacancy type. The surface vacancies are named as V_S, V_{Ni}, and V_{Ni-S} for S-, Ni-, and Ni/S-vacancies, respectively, where the integer n_i stands for the total number of vacancies associated with an element, i (i.e., S or Ni) removed from the catalyst, and μ_i indicates the chemical potential of the element, i. The chemical potentials of the constituent elements in $NiPS_3$ are thermodynamically constrained to model experimental growth conditions. The equilibrium conditions of the chemical potentials for the growth of $NiPS_3$ are defined as:

$$\mu_{Ni} + \mu_P + 3\mu_S = E[NiPS_3] \tag{7}$$

Here, μ_i represents the chemical potential of element i. Using the definition of the formation energy, $\Delta H_f(NiPS_3) = E[NiPS_3] - (E[Ni] + E[P] + 3E[S])$, the equilibrium conditions of chemical potentials can be expressed as:

$$\Delta H_f(NiPS_3) = (\mu_{Ni} - E[Ni]) + (\mu_P - E[P]) + 3(\mu_S - E[S]) = \Delta\mu_{Ni} + \Delta\mu_P + 3\Delta\mu_S \tag{8}$$

Here, $\Delta\mu_i = \mu_i - E_i$ is the change in the chemical potential of an element, i, relative to its bulk phase energy. Specifically, μ_i is the chemical potential of the element, i, and E_i is the DFT-calculated total energy per formula unit for its bulk phase compound. Notably, μ_i, is predicted from the afore-mentioned relationship of μ_i, E_i, and $\Delta\mu_i$, while E_i is computed by the DFT method and $\Delta\mu_i$ is obtained for a specified point in Fig. 2a.

Since it is presumed that the bulk phases of Ni, P, and S elements are not formed, the following conditions must also be satisfied:

$$\Delta\mu_{Ni} \le 0 \tag{9}$$

$$\Delta\mu_P \le 0 \tag{10}$$

$$\Delta\mu_S \le 0 \tag{11}$$

Following the same logic, bulk phases that compete with $NiPS_3$, such as Ni_3S_2, Ni_3S_4, NiS_2, P_2S_5, P_2S_7, P_4S_7, and NiPS, must also satisfy the following constraints:

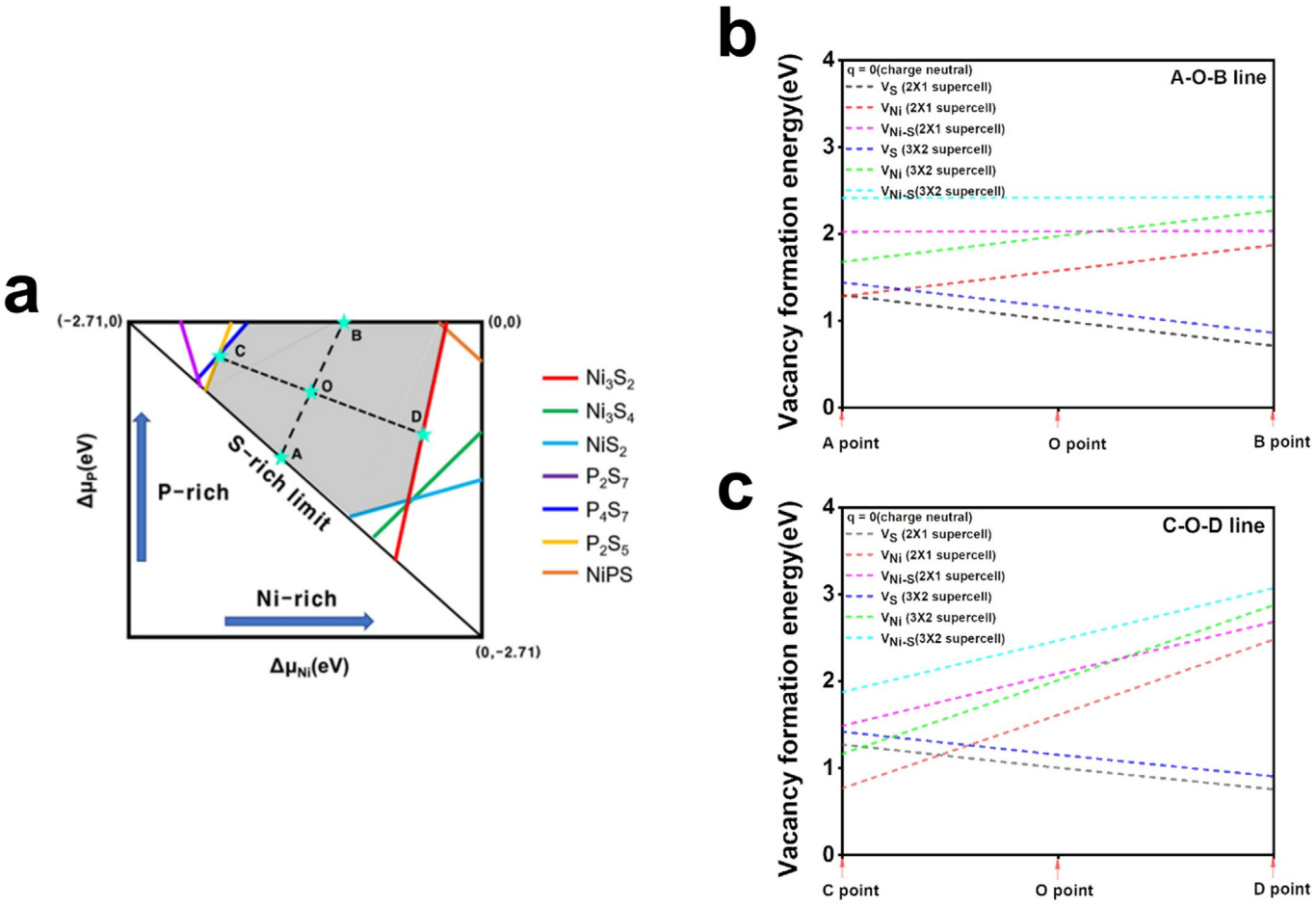

Fig. 2. (a) Chemical potential space (in gray color) of three constituent elements, Ni, S, and P, enabling the stable formation of two-dimensional $NiPS_3$ monolayer under the consideration of relevant constraints. (b) The formation energies (in eV) of V_S, V_{Ni}, and V_{Ni-S} at two selected sets of points, namely (b) A-O-B and (c) C-O-D, within the chemical potential space defined in (a).

$$\Delta H_f(Ni_3S_2) \geq 3\Delta\mu_{Ni} + 2\Delta\mu_S \quad (12)$$

$$\Delta H_f(Ni_3S_4) \geq 3\Delta\mu_{Ni} + 4\Delta\mu_S \quad (13)$$

$$\Delta H_f(NiS_2) \geq \Delta\mu_{Ni} + 2\Delta\mu_S \quad (14)$$

$$\Delta H_f(P_2S_7) \geq 2\Delta\mu_P + 7\Delta\mu_S \quad (15)$$

$$\Delta H_f(P_4S_7) \geq 4\Delta\mu_P + 7\Delta\mu_S \quad (16)$$

$$\Delta H_f(P_2S_5) \geq 2\Delta\mu_P + 5\Delta\mu_S \quad (17)$$

$$\Delta H_f(NiPS) \geq \Delta\mu_{Ni} + \Delta\mu_P + \Delta\mu_S \quad (18)$$

Table 1 lists all the DFT-calculated formation energies as defined by the aforementioned equations. The stable formation of the two-dimensional $NiPS_3$ monolayer was considered under the constraints outlined in Fig. 2a, which defines the range of chemical potentials of the constituent elements. To examine the vacancy formation energies at different points, two sets of three points were selected linearly within the defined chemical potential range.

In the surface vacancy formation scenarios, the incorporated vacancies were presumed to be neutral, regardless of the vacancy type. For mono-vacancy scenarios, it is noteworthy that the presence of charged vacancies is essentially impossible in terms of the charge neutrality of the designed model systems. For di-vacancy scenario (Ni/S-vacancy), the total charge of the Ni–S vacancy pair should be neutral, despite the possibility of oppositely charged states for the Ni and S vacancies. More importantly, the charge assignment of individual vacancies in the $NiPS_3$ catalyst with a surface di-vacancy would not affect core conclusions on its computational performance parameters drawn below, considering the characteristics of the performance depending on the electronic structures of catalyst surfaces. Notably, the vacancy formation energy may rely on the charge states assigned in each vacancy for the di-vacancy scenario. However, this study verifies that the formation of the neutrally charged surface di-vacancy would be relatively feasible as compared with other two-dimensional materials, such as C-vacancy in graphene and S-vacancy in MoS_2 (Fig. 2). Therefore, it is not necessary to further investigate the thermodynamic stability for various di-vacancy scenarios with positively/negatively charged vacancies.

Electronic analysis: To elucidate the impact of vacancies of the electronic structure of $NiPS_3$ monolayer, *p*-band centers (ε_P) of S and P atoms were calculated using the following equation:

$$\varepsilon_P = \frac{\int_{-\infty}^{E_F} \varepsilon\rho_p d\varepsilon}{\int_{-\infty}^{E_F} \rho_p d\varepsilon} \quad (19)$$

Here, E_F represents the Fermi level (which, for simplicity, we set to 0 eV), ρ_p stands for the local density of states (LDOS), and ε is an energy width of the *p* orbital. In addition, the LDOS of each monolayer model was examined to understand the vacancy-dependent binding strength of protons adsorbed electrochemically onto the catalyst surfaces.

Table 1
DFT-calculated formation energies of $NiPS_3$ and its competing phases for the chemical potentials space of three constituent elements.

Compound	Formation energy (eV)
$NiPS_3$	−2.71
Ni_3S_2	−2.20
Ni_3S_4	−2.69
NiS_2	−1.05
P_2S_5	−1.22
P_2S_7	−1.20
P_4S_7	−2.30
NiPS	−1.04

3. Results and discussion

This study analyzes the impact of defects on the catalytic stability and performance parameters of $NiPS_3$, to better understand the potential effects of defective surfaces that may be generated during experimental catalyst development processes. Surface defects, represented by vacancies, are systematically designed, and considered with variations in the type of vacancy, as illustrated in Fig. 1. The first section of the study discusses the thermodynamic stability of catalyst surfaces with various mono- or di-vacancies with the aim of assessing the feasibility of surface vacancy formation. The subsequent section further analyzes the introduction of thermodynamically feasible vacancies on the catalyst surfaces to decipher the effect of local vacancies on catalytic HER activity.

Notably, the surface vacancies designed in this study may be deactivated by various resources, including the adsorption of hydroxyl ions or other impurity ions on vacant sites. However, it is noteworthy that the main goal of this study is to understand the catalytic performance associated with the dissociative adsorption of H_2O and subsequent hydrogen adsorption on distinct surface vacancies of $NiPS_3$ monolayer. A deep analysis of the potential degradation of the vacant sites is therefore beyond this work. Nonetheless, we explored for a potential degradation arising from the adsorption of hydroxyl ions on S vacancy exposed on the surface of $NiPS_3$ monolayer, because the hydroxyl ions are involved during the process of the dissociative adsorption of H_2O. The adsorption free energies of a hydroxyl ion on the S vacancy sites of S mono-vacancy and NiS di-vacancy scenarios are revealed to be positive, indicating the thermodynamic instability of the adsorption behaviors (Fig. S17). The small atomic size of oxygen relative to sulfur seems to significantly lower the electronic overlap with local surface atoms, leading to the weakening of the adsorption strength. Therefore, it is evident that the hydroxyl ions, produced by the dissociative adsorption of H_2O on the catalyst surface, would not trigger the degradation of catalytically active vacancies.

3.1. Assessing thermodynamic feasibility of vacancy formation

The vacancy formation energies of three distinctive vacancy types, namely V_S, V_{Ni}, and V_{Ni-S}, were investigated to unravel their relative thermodynamic stability (Figs. 2b and c). Notably, the most stable configuration was identified by examining the vacancy formation thermodynamics of all available configurations for each vacancy type. An analysis of the vacancy formation energies of $NiPS_3$ monolayer at two different three-point sets (i.e., A-O-B and C-O-D) reveals the relative thermodynamic stability on the three distinctive defective surfaces. The $NiPS_3$ monolayer with V_S is predicted to be the most plausible defective surface over the almost entire chemical potential space for the A-O-B line and at about 75% of the chemical potential space for the C-O-D line. In a previous experimental study, Tong *et al.* highlighted that two-dimensionally layered $NiPS_3$ structures contained a majority of vacancies in S sites with a minor number of Ni-induced vacancies, which is in great agreement with our computational analysis [32]. This validates the reliability of our computational protocol for accurately predicting vacancy formation thermodynamics. Furthermore, the $NiPS_3$ monolayer is predicted to preferentially form mono-vacancy rather than di-vacancy over the entire chemical potential ranges for both the descriptive points, A-O-B and C-O-D, indicating a potentially weakened stability of di-vacancy arising from a repulsive interaction between neighboring vacancies. Notably, the discussed trend in the vacancy formation thermodynamics is independent of the surface coverage of vacancies.

The feasibility of S vacancy formation in $NiPS_3$ is further evaluated by comparing its thermodynamics with the formation of defective surfaces in various two-dimensional materials. The formation energies of C-vacancy in graphene [33] and S-vacancy in MoS_2 [34] have been reported to be 7.69 and 5.85 eV, respectively, which are higher than the vacancy formation energies (0.80–2.96 eV) in $NiPS_3$ (Figs. 2b and c). This implies that vacancy formation in $NiPS_3$ structures would be relatively feasible under experimental conditions. Therefore, understanding the effect of all

surface vacancies (i.e., V_S, V_{Ni}, and $V_{Ni–S}$) on HER performance is crucial in suggesting a desired direction of defect-induced surface modulation.

3.2. Two key steps of HER

HER is initiated under alkaline conditions by the dissociative adsorption of a water molecule on the surface of a catalyst. This process produces a proton and a hydroxide anion, which are subsequently adsorbed on the catalyst surfaces of the cathode and anode, respectively [35,36]. To analyze the HER activity and resultant performance, it is useful to consider the two main steps involved: (i) the dissociative adsorption of a water molecule on a $NiPS_3$ monolayer and (ii) the electrochemical adsorption of the dissociated proton on the $NiPS_3$ monolayer. The type of vacancies present in the $NiPS_3$ monolayer can significantly influence the efficiency of these steps and therefore affect the overall performance of the HER reaction.

3.3. Vacancy-induced enhancement in HER: dissociative adsorption of water molecule

1st step of the dissociative adsorption of a water molecule: In the first step of the dissociative adsorption, a water molecule goes through the physisorption on an active site of each catalyst surface, triggering dissociation. The energetic stabilization of this process is calculated to range from −0.14 to −0.55 eV for $NiPS_3$ monolayer models presented in this study (Fig. 3). The Gibbs free energy change resulting from the physical adsorption thermodynamics, including vibrational and entropic contributions, is determined to range from −0.10 to 0.87 eV for all models (Fig. S1). Notably, the active site is chosen based on the identification of a globally stable adsorption site among all available sites. Clearly, the pristine $NiPS_3$ monolayer exhibits physical adsorption primarily through an electrostatic interaction of P (catalyst) – O (water) with negligible contributions from interactions between S (catalyst) and H (water) (Figs. S2a and S2e). The centrally positioned Ni atoms do not participate in the physical adsorption owing to geometrical hindrance, despite their electron-donating nature (Figs. S1, S2a, and S2e).

Further analysis reveals the effect of vacancies in the catalyst surface on the physical adsorption strength of a water molecule (Figs. S1 and S2). The incorporation of S mono-vacancy is found to have a beneficial effect, reducing the Gibbs free energy change by 0.090–0.102 eV depending on the surface coverage of the vacancy, due to a fundamental change in the binding characteristics (Figs. S1, S2b, and S2f). This is because the removal of an electron-withdrawing S atom exposes the geometrically hindered Ni atoms, facilitating a significant electronic transfer from the electron-donating Ni atoms to the O atom of the adsorbed water molecule through an S-substitution-like formation of the O atom (Figs. S2b and S2f). In contrast, the removal of a centrally positioned Ni atom in the monolayer has a detrimental effect on the electronic transfers between the monolayer and water, exhibiting a relatively small visual cloud compared to the pristine monolayer (Figs. S2c and S2g). Notably, previous studies on the HER activity of defective MoS_2 monolayers have also highlighted that the performance of S vacancy configuration is superior

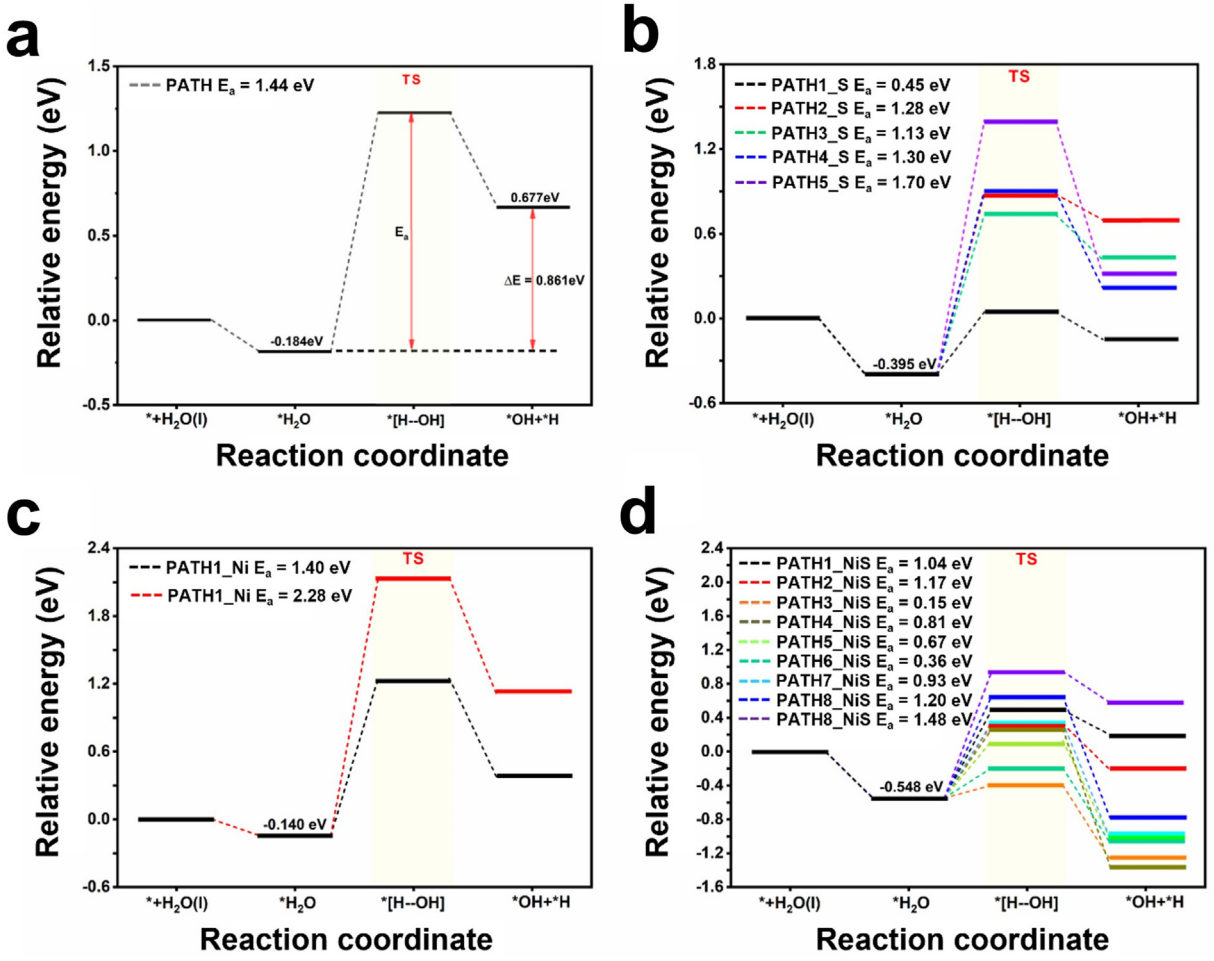

Fig. 3. DFT-calculated relative energy profiles (with computed transition state (TS) levels) associated with the dissociative adsorption of a water molecule on two-dimensional $NiPS_3$ monolayer models with (a) no vacancy, (b) V_S, (c) V_{Ni}, and (d) $V_{Ni–S}$. All available pathways associated with the dissociative adsorption are considered for each vacancy type.

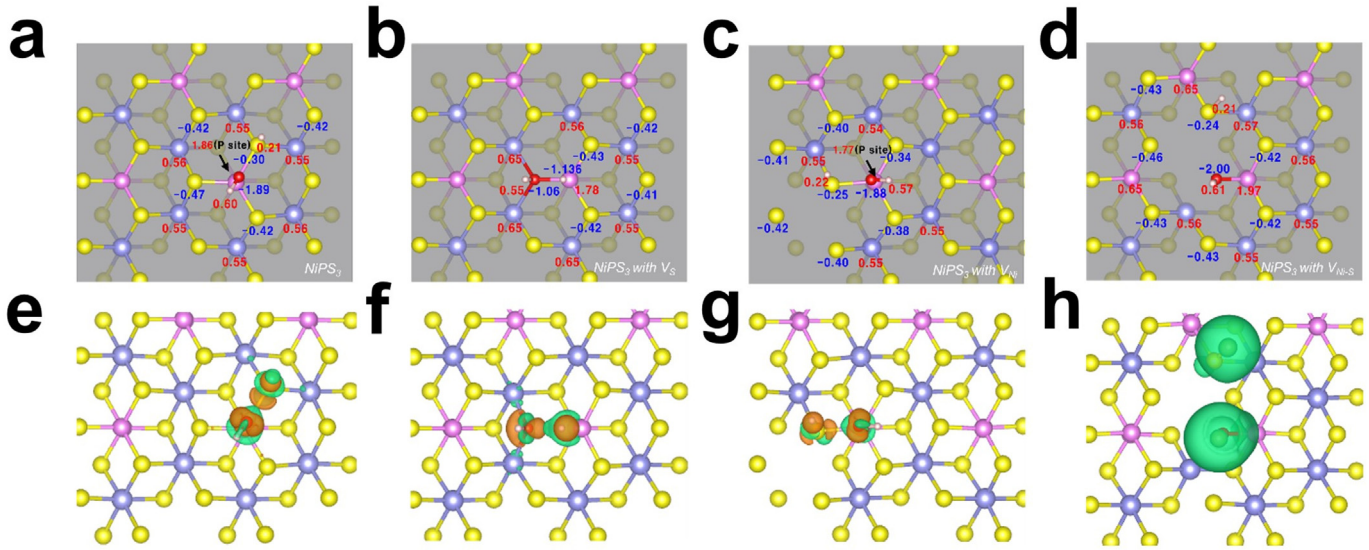

Fig. 4. The atomic charges and charge density changes predicted during the dissociation of a water molecule adsorbed on a $NiPS_3$ monolayer with (a, e) no vacancy, (b, f) S mono-vacancy, (c, g) Ni mono-vacancy, or (d, h) NiS di-vacancy. In (e–h), areas with orange and green in color indicate the electron-rich, and electron-deficient areas, respectively. Atoms with blue, pink, yellow, red, and white in color depict nickel, phosphorus, sulfur, oxygen, and hydrogen, respectively.

to that of transition metal vacancy configuration [37–39]. Surprisingly, the co-removal of neighboring Ni and S atoms to form a NiS di-vacancy dramatically improves the physical adsorption thermodynamics with a lower free energy change than the S mono-vacancy configuration, despite the co-existence of a detrimental Ni vacancy (Fig. S1). Deeper analysis reveals that the additional removal of a Ni atom neighboring the S vacancy enables hydrogen atoms of the water molecule to form hydrogen bonds with neighboring S atoms through self-reorientation (solid circles with red color in Fig. S2h). This is the main reason for the unexpected stabilization of the physical adsorption of the water molecule.

2nd step of dissociative adsorption of water molecule: The second step involves the subsequent dissociation of the physically adsorbed water molecule into a pair of a proton and a hydroxide anion. The impact of vacancy-induced dissociation is analyzed from both thermodynamic and kinetic points of view (Fig. 3 and Table 2). This chemical decomposition process is completed by adsorbing each decomposed species onto its stable site. It is quite clear to see that the Gibbs free energy change and relevant transition state associated with dissociation strongly depend on the vacancy type and reaction pathway. Detailed pathways associated with dissociation are described in Figs. S3–S6. The dissociation of a water molecule adsorbed on pristine $NiPS_3$ monolayer has a Gibbs free energy change of 0.88 eV, which is relatively high as compared with 0.26, 0.57, and −0.91 eV (at their most stable pathways) with the incorporation of V_S, V_{Ni}, and V_{Ni-S} on the monolayer, respectively. Furthermore, six out of the nine possible dissociation pathways for $NiPS_3$ monolayer with V_{Ni-S} are thermodynamically exothermic, with Gibbs free energy changes ranging between −0.37 and −0.91 eV. These findings indicate that all the defective sites would play a crucial role in decomposing the adsorbed water molecule, with an emphasis on the synergistic effect of neighboring vacancies.

Under alkaline conditions, the dissociative adsorption of water molecules on a catalyst surface is well-known to be the rate-determining step for the catalytic HER [40–44]. Further analysis of the kinetic behavior associated with the dissociation of water molecules adsorbed on a $NiPS_3$ monolayer reveals that the thermodynamic enhancement induced by vacancies can be boosted by kinetic benefits (Fig. 3 and Table 2). Specifically, the activation energy barriers for the S mono-vacancy configuration range from 0.45 to 1.70 eV, depending on the pathways, with the most stable pathway having an activation energy barrier of **0.45 eV**. For the Ni mono-vacancy configuration, the most stable pathway has a lower activation energy barrier (**1.40 eV**) than the pristine $NiPS_3$ monolayer. Interestingly, the NiS di-vacancy configuration, which shows the most significant enhancement in the reaction thermodynamics, has activation energy barriers ranging from 0.15 to 1.48 eV, depending on the pathway, with the most stable pathway having an activation energy barrier of **0.81 eV**. More importantly, the second and third most stable pathways, which have negative Gibbs free energy changes, have the lowest activation energy barriers (**0.15** and **0.36 eV**, respectively) among all the possible reaction scenarios described in this study.

Consequently, the dissociative adsorption of a water molecule on a $NiPS_3$ monolayer can be most efficiently achieved by the incorporation of a NiS di-vacancy. (i) NiS di-vacancy can enhance the activation process of the physical adsorption of the water molecule on the

Table 2
Gibbs free energy changes (ΔG_{dis}) for the dissociation of a water molecule adsorbed on pristine $NiPS_3$ monolayer model and its defective models and DFT-calculated activation energy barriers (E_a) for the reaction. (*: the most stable pathway).

Pristine material	ΔG_{dis} (eV)	E_a (eV)
PATH	0.88	**1.44**
S mono-vacancy	**ΔG_{dis} (eV)**	**E_a (eV)**
PATH1_S*	0.26	**0.45**
PATH2_S	1.07	1.28
PATH3_S	1.25	1.13
PATH4_S	0.58	1.30
PATH5_S	0.72	1.70
Ni mono-vacancy	**ΔG_{dis} (eV)**	**E_a (eV)**
PATH1_Ni*	0.57	**1.40**
PATH2_Ni	1.23	2.28
NiS di-vacancy	**ΔG_{dis} (eV)**	**E_a (eV)**
PATH1_NiS	0.68	1.04
PATH2_NiS	0.20	1.17
PATH3_NiS	−0.86	0.15
PATH4_NiS*	−0.91	**0.81**
PATH5_NiS	−0.62	0.67
PATH6_NiS	−0.67	0.36
PATH7_NiS	−0.62	0.93
PATH8_NiS	−0.37	1.20
PATH9_NiS	1.06	1.48

monolayer with Gibbs free energy changes close to zero. (ii) The subsequent dissociation of the water molecule adsorbed on the monolayer can be further assisted by the incorporated NiS di-vacancy, which offers both thermodynamic and kinetic benefits. *From a thermodynamic perspective*, the NiS di-vacancy configuration dramatically lowers the reaction thermodynamics, even producing negative Gibbs free energy changes (i.e., exothermic reaction) for several pathways. This implies that the di-vacancy configuration utilizing the synergistic effect of neighboring vacancies would be best suited for the stable formation of an electrochemically dissociated proton. *From a kinetic perspective*, the S mono-vacancy configuration is predicted to have the most significant reduction in the activation energy barrier for the dissociation of a water molecule adsorbed on the $NiPS_3$ monolayer when considering the most stable pathway for each vacancy configuration. This trend is however not consistent with the results from other (promising) metastable pathways. The NiS di-vacancy configuration is particularly highlighted to have the lowest activation energy barriers through pathways which offer the secondly and thirdly most significant thermodynamic benefits. This implies that the dissociation of a water molecule adsorbed on the NiS di-vacancy configuration can be kinetically boosted once the global-minimum active site is already occupied by another water molecule. Considering the importance of dissociative water adsorption as a key step for determining HER kinetics together with the highlighted thermodynamic benefits, the NiS di-vacancy configuration is concluded to be the most desirable for the dissociative adsorption of a water molecule on a $NiPS_3$ monolayer.

Origin of vacancy-induced enhancement in the dissociative adsorption of water molecule (Fig. 4): The dissociated species, namely proton and hydroxide anion, play a crucial role in stabilizing the electronic structure of the $NiPS_3$ monolayer with V_S or $V_{Ni–S}$, through the S-substitution-like formation of a hydroxide anion on the monolayer with active electronic transfers. Under the NiS di-vacancy configuration, both the S and Ni vacancies are even rigorously stabilized by hydroxide anion and proton, respectively, leading to exothermic dissociation thermodynamics. In contrast, the $NiPS_3$ monolayer with no vacancy or with V_{Ni} (i.e., the removal of Ni atom deep inside the monolayer) exhibits surficial electronic transfers of P (catalyst) – O (water) and S (catalyst) – H (water), which results in relatively weak stabilization in the dissociation thermodynamics. Therefore, the vacancy-induced enhancement in the dissociative adsorption of a water molecule is mainly attributed to the stabilization of the dissociated species through active electronic transfers between the catalyst and water molecule.

3.4. Vacancy-induced enhancement in HER: electrochemical adsorption of proton

The activation of a dissociated proton on the surface of a catalyst is a crucial step in determining the HER activity, through either Heyrovsky or Tafel scheme associated with the subsequent evolution of a hydrogen molecule. The effect of the afore-mentioned vacancies on the adsorption of hydrogen on $NiPS_3$ monolayer is therefore investigated to assess the potential of defect engineering in enhancing HER activity (Figs. 5

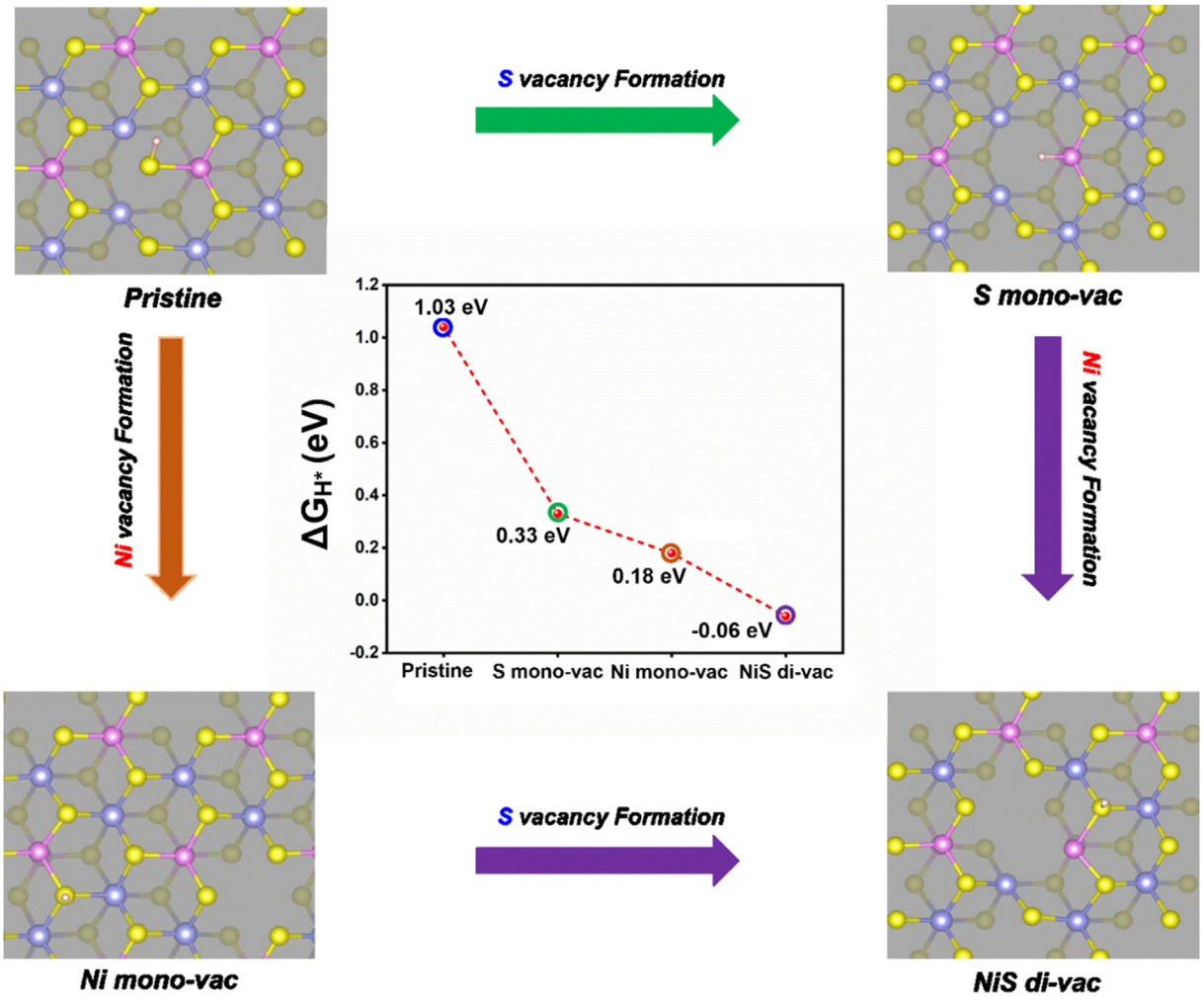

Fig. 5. Gibbs free energy changes associated with the adsorption of a hydrogen atom on two-dimensional $NiPS_3$ monolayer ((2×1) supercell) with no vacancy or with vacancies (i.e., V_S, V_{Ni}, and $V_{Ni–S}$). Atoms with blue, pink, yellow, and white in color depict nickel, phosphorus, sulfur, and hydrogen, respectively.

and S7–S12). For a reference system, the pristine $NiPS_3$ monolayer exhibits a relatively weak hydrogen adsorption, with free energy changes of 1.54 and 1.03 eV associated with the hydrogen adsorption at P and S sites, respectively (Figs. 5, S7a, S8a, and S9). This intrinsic adsorption strength is compared to that of Pt, the best-known HER catalyst, which has a mild free energy change (−0.09 eV), causing a thermodynamic barrier against subsequent evolution of a hydrogen molecule [45]. Therefore, investigating the effect of vacancies on hydrogen adsorption is crucial for understanding their potential in enhancing the overall HER activity.

The incorporation of a vacancy in $NiPS_3$ monolayer however drastically enhances the HER activity (Figs. 5 and S7b–S7d). The incorporation of S mono-vacancy enables the hydrogen adsorption thermodynamics to range between 0.32 and 1.63 eV, indicating a potential benefit in the HER activity for Ni, P1, and S3 adsorption sites (Figs. 5, S7b, S8b, and S10). Moreover, the Ni mono-vacancy configuration exhibits better hydrogen adsorption thermodynamics for all S adsorption sites, with free energy changes closer to zero than the pristine $NiPS_3$ monolayer (Figs. 5, S7c, S8c, and S11). Most impressively, the NiS di-vacancy configuration has multiple adsorption sites near the hydrogen adsorption thermodynamics (−0.09 eV) of a reference catalyst, Pt, with an emphasis on the presence of an ideally suitable adsorption site, namely S6 (Figs. 5, S7d, S8d, and S12). This active site consistently exhibits the hydrogen adsorption thermodynamics within −0.09 to 0.09 eV, regardless of the vacancy coverage. This suggests that achieving hydrogen adsorption activity of $NiPS_3$ monolayer comparable to that of Pt catalyst requires state-of-the-art design of its local surface geometry.

The impact of vacancies on the HER activity is further highlighted by well-established volcano plots depicting the correlation between hydrogen adsorption thermodynamics and exchange current density (Fig. 6) [46,47]. The exchange current density of the pristine $NiPS_3$ monolayer with weak hydrogen binding unambiguously increases with the incorporation of a vacancy configuration, demonstrating the best performance on S5 and S6 sites of NiS di-vacancy configuration. Notably, these sites exhibit performance parameters comparable to or even higher than the well-established best catalyst, Pt (111) surface, although considering the unavailability of information on other crucial parameters, such as structural durability [48]. This underscores the consistency in the trend of the thermodynamic (i.e., hydrogen adsorption strength) and kinetic (i.e., exchange current density) properties depending on the type of vacancy.

Origin of vacancy-induced enhancement in hydrogen adsorption thermodynamics: The local DOS (LDOS) of the *p* orbital for a specific element was further analyzed alongside crystal orbital Hamiltonian population (COHP) analysis to understand the influence of the vacancy configuration on hydrogen adsorption thermodynamics (Figs. 7, S13, S14, and S15). It is noteworthy that the computational protocol employed in this study accurately predicts the electronic DOS of the pristine $NiPS_3$ monolayer with a deviation of 0.01–0.04 eV from its experimental (1.60 eV) and computed (1.63 eV) bandgaps in previous studies, thus validating its reliable predictive ability (Fig. S13a) [49–51]. Moreover, incorporating a mono- or di-vacancy is predicted to decrease the bandgap of the pristine $NiPS_3$ monolayer, indicating vacancy-induced enhancement in the electronic conductivity, with Ni element removal having a more significant impact (Fig. S13) [52].

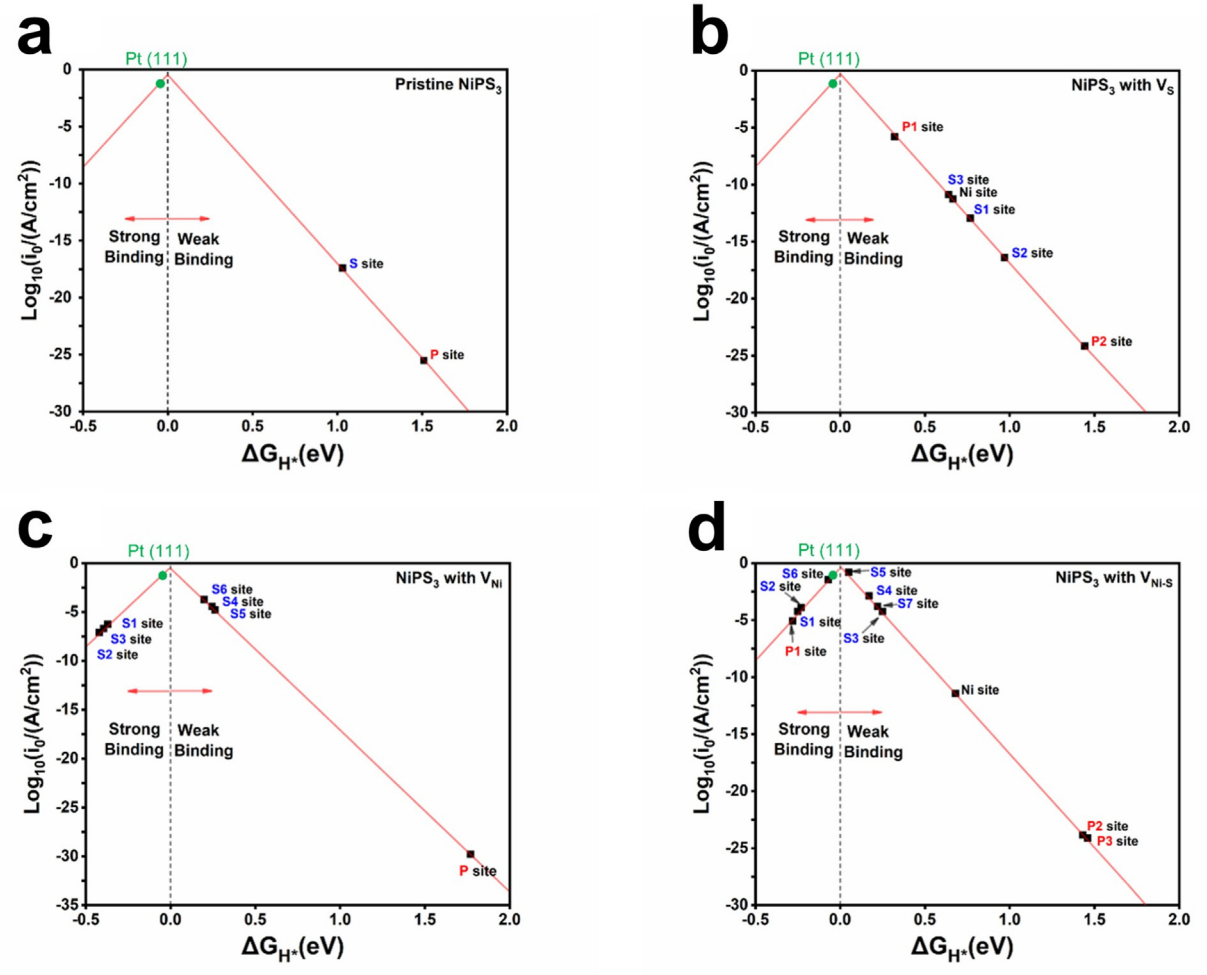

Fig. 6. The volcano plots of two-dimensional $NiPS_3$ monolayers ((2 × 1) supercell) with (a) no vacancy or with vacancies (i.e., (b) V_S, (c) V_{Ni}, and (d) V_{Ni-S}).

The LDOS of active P sites, namely P, P1, P, or P1 sites for $NiPS_3$ monolayer with no vacancy, V_S, V_{Ni}, or V_{Ni-S} in Fig. S8, respectively, reports *p*-band centers of −5.64, −4.27, −5.70, and −4.00 eV for the $NiPS_3$ monolayer with no vacancy, V_S, V_{Ni}, or V_{Ni-S}, respectively (Fig. 7e). Further analysis of the correlation between hydrogen adsorption thermodynamics (ΔG_{H^*}) on the active site and *p*-band center reveals that a higher *p*-band center would result in stronger hydrogen adsorption, implying a decrease in the contribution of the anti-bonding orbital (Fig. 7f) [53–55]. From the chemical point of view, COHP, which partitions the band-structure energy into orbital-pair interactions, is defined as bond-weighted DOS between a pair of adjacent atoms. The integrated projected COHP (IpCOHP) shows the contribution of a specific (chemical) bond to the bond-structure energy. Therefore, a COHP diagram indicates bonding and antibonding contributions to the band-structure energy and IpCOHP describes the strength of the bond. Specifically, the integrated COHP analysis (i.e., –IpCOHP) consistently shows higher –IpCOHP values (and hence shorter P–H bond lengths) for stronger hydrogen adsorption (Fig. 7f). These findings suggest that the vacancy dependence of hydrogen adsorption strength originates from distinct characteristics of local electronic structures near the vacancies. These correlations further apply to active S sites, as evidenced by the

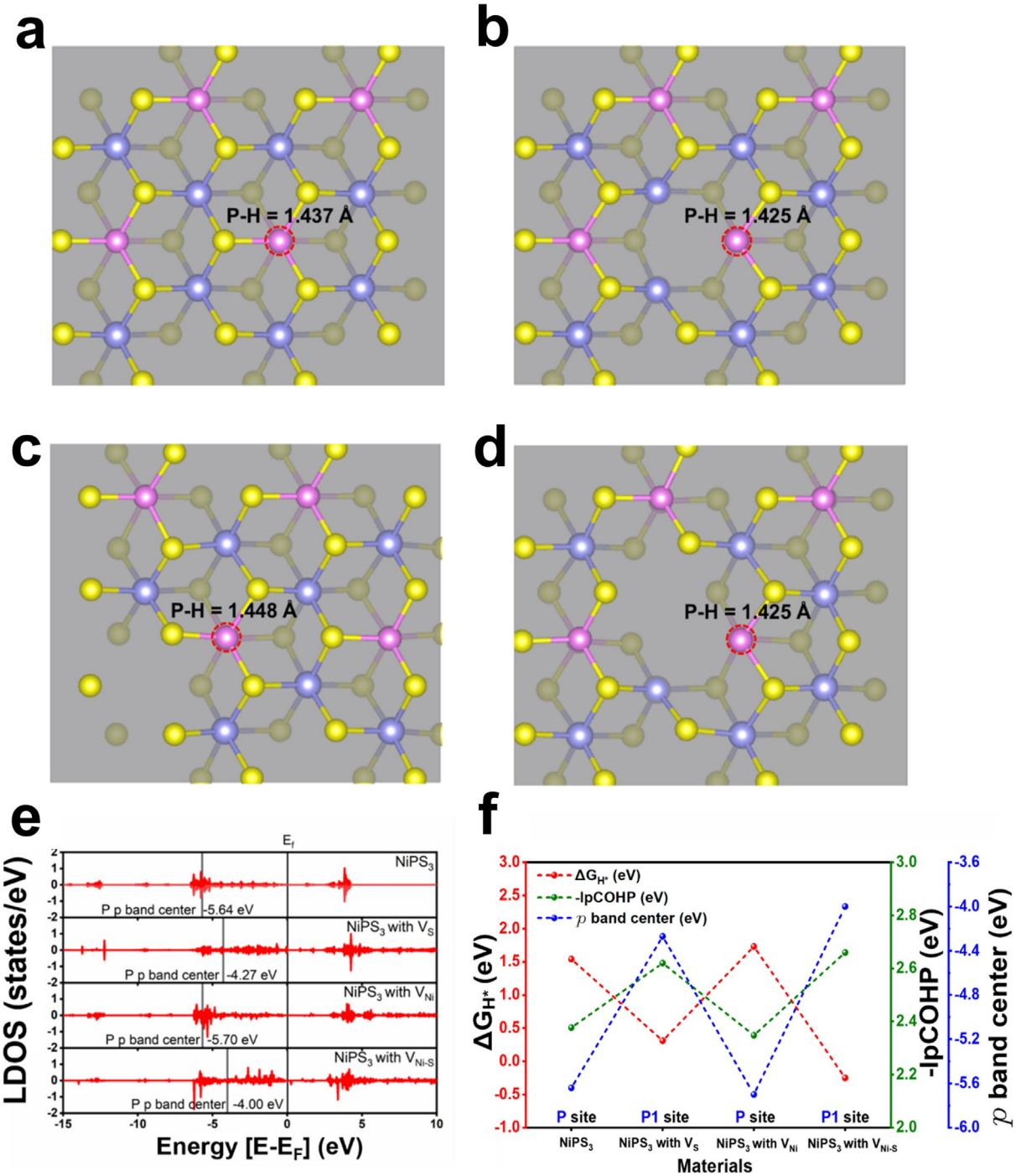

Fig. 7. Top views associated with the hydrogen adsorption for two-dimensional $NiPS_3$ monolayers ((2 × 1) supercell) with (a) no vacancy or with vacancies (i.e., (b) V_S, (c) V_{Ni}, and (d) V_{Ni-S}). (e) The LDOS (*p* orbital) of an active P site for the hydrogen adsorption with a depiction of *p* band center for each of them and (f) resultant correlations of the free energy change of the hydrogen adsorption on each active P site with –IpCOHP and *p* band center.

analysis of DFT-calculated *p*-band centers and –IpCOHP values for active S sites (Figs. S14 and S15). However, an exception to the above correlation is observed in the Ni mono-vacancy configuration, where unexpectedly lower –IpCOHP values are observed for stronger hydrogen adsorption sites (i.e., S1–S3 sites) (Fig. S15b). This suggests that hydrogen adsorption behaviors at these sites are predominantly contributed by a couple of hydrogen bonds with S atoms that are not directly involved in the S–H bonding (Fig. S16).

One might suspect an experimental feasibility of the high-performance catalyst, $NiPS_3$ monolayer with NiS di-vacancy, designed in this study. However, the experimental development of NiS di-vacancy on the surface of the $NiPS_3$ monolayer was already proven to be possible in a previous study [32]. Specifically, they employed a simple ball-milling treatment with ultrasonication to create NiS di-vacancies on nickel and sulfur sites of the $NiPS_3$ nanosheets. This indicates that the generation scenario of the NiS di-vacancy described in this study would be an experimentally feasible scenario, beyond a product of ideal model design.

4. Conclusions

This study utilized first-principles calculations to investigate the impact of a defect engineering approach on the HER activity of a $NiPS_3$ monolayer catalyst. Three different types of vacancies (S-, Ni-, and NiS-vacancies) were designed to explore their influence on the basal plane of the monolayer during a multi-step mechanism involving the dissociative adsorption of a water molecule and subsequent electrochemical adsorption of the dissociated proton. The investigation revealed that the co-formation of vacancies in both Ni and S sites would be the most effective in enhancing the catalytic performance of the monolayer.

The study highlighted conclusive remarks on the core observation. First, the S-substitution-like physisorption of a water molecule on a vacant S site, followed by the dissociative occupation of OH and H into vacant sites of S and Ni elements, was the key resource for the reaction thermodynamics boosted by the NiS di-vacancy configuration. Second, the kinetic benefit of the NiS di-vacancy configuration was rationalized by exceptionally low activation energy barriers at a couple of metastable but thermodynamically exothermic pathways of the dissociative adsorption of a water molecule. Third, the vacancy dependence of the hydrogen adsorption strength was verified to originate from the distinct characteristics of the local electronic structures near the vacancies. Specifically, the NiS di-vacancy configuration showed the highest (least) contribution of the bonding (anti-bonding) orbitals to the monolayer-H bond. Overall, these findings provide insight into desired defect engineering for transition metal phosphorus chalcogenides with high HER activities. This study will be further extended to other chalcogenide monolayers in future work with the aim of generalizing the core observations associated with the exceptional enhancement in the performance of $NiPS_3$ monolayers arising from the incorporation of di-vacancy.

Author contributions

Conceptualization, K.C.K.; Methodology, K.C.K. and H.G.H.; Investigation, H.G.H., J.W.C., and M.S.; Writing – Original Draft, K.C.K. and H.G.H.; Writing – Review & Editing, K.C.K.; Funding Acquisition, K.C.K.; Supervision, K.C.K.

Declaration of competing interest

The authors declare no competing financial interest.

Acknowledgment

This work was supported by the National Research Foundation of Korea (NRF), funded by the Ministry of Science and ICT (NRF-2020R1A2C1009177). This work was also supported in part by Human Resources Development Program of the Korea Institute of Energy Technology Evaluation and Planning (KETEP) grant funded by the Ministry of Trade, Industry and Energy, Republic of Korea (No. RS-2023-00237035).

Appendix A. Supplementary data

Supplementary data to this article can be found online at https://doi.org/10.1016/j.esci.2023.100204.

References

[1] G. Zhao, K. Rui, S.X. Dou, W. Sun, Heterostructures for electrochemical hydrogen evolution reaction: a review, Adv. Funct. Mater. 28 (2018) 1803291.
[2] F. Safizadeh, E. Ghali, G. Houlachi, Electrocatalysis developments for hydrogen evolution reaction in alkaline solutions–a review, Int. J. Hydrogen Energy 40 (2015) 256–274.
[3] Z. Liang, X. Zhong, T. Li, M. Chen, G. Feng, DFT study on the hydrogen evolution reaction for different facets of Co_2P, ChemElectroChem 6 (2019) 260–267.
[4] W. Qian, Z. Chen, J. Zhang, L. Yin, Monolayer $MoSi_2N_{4-x}$ as promising electrocatalyst for hydrogen evolution reaction: a DFT prediction, J. Mater. Sci. Technol. 99 (2022) 215–222.
[5] Y. Liu, B. Huang, X. Hu, Z. Xie, Surfactant-assisted hydrothermal synthesis of nitrogen doped Mo_2C@ C composites as highly efficient electrocatalysts for hydrogen evolution reaction, Int. J. Hydrogen Energy 44 (2019) 3702–3710.
[6] G. Ye, Y. Gong, J. Lin, B. Li, Y. He, S.T. Pantelides, W. Zhou, R. Vajtai, P.M. Ajayan, Defects engineered monolayer MoS_2 for improved hydrogen evolution reaction, Nano Lett. 16 (2016) 1097–1103.
[7] J. Xiong, W. Cai, W. Shi, X. Zhang, J. Li, Z. Yang, L. Feng, H. Cheng, Salt-templated synthesis of defect-rich MoN nanosheets for boosted hydrogen evolution reaction, J. Mater. Chem. A 5 (2017) 24193–24198.
[8] H. Li, C. Tsai, A.L. Koh, L. Cai, A.W. Contryman, A.H. Fragapane, J. Zhao, H.S. Han, H.C. Manoharan, F. Abild-Pedersen, Activating and optimizing MoS_2 basal planes for hydrogen evolution through the formation of strained sulphur vacancies, Nat. Mater. 15 (2016) 48–53.
[9] J. Zhang, C. Zhang, Z. Wang, J. Zhu, Z. Wen, X. Zhao, X. Zhang, J. Xu, Z. Lu, Synergistic interlayer and defect engineering in VS_2 nanosheets toward efficient electrocatalytic hydrogen evolution reaction, Small 14 (2018) 1703098.
[10] C. Tsai, H. Li, S. Park, J. Park, H.S. Han, J.K. Nørskov, X. Zheng, F. Abild-Pedersen, Electrochemical generation of sulfur vacancies in the basal plane of MoS_2 for hydrogen evolution, Nat. Commun. 8 (2017) 15113.
[11] Y. Liu, Y. Chen, Y. Tian, T. Sakthivel, H. Liu, S. Guo, H. Zeng, Z. Dai, Synergizing hydrogen spillover and deprotonation by the internal polarization field in a MoS_2/$NiPS_3$ vertical heterostructure for boosted water electrolysis, Adv. Mater. 34 (2022) 2203615.
[12] S. Wang, B. Xiao, S. Shen, K. Song, Z. Lin, Z. Wang, Y. Chen, W. Zhong, Cobalt doping of $FePS_3$ promotes intrinsic active sites for the efficient hydrogen evolution reaction, Nanoscale 12 (2020) 14459–14464.
[13] Z. Yu, J. Peng, Y. Liu, W. Liu, H. Liu, Y. Guo, Amine-assisted exfoliation and electrical conductivity modulation toward few-layer $FePS_3$ nanosheets for efficient hydrogen evolution, J. Mater. Chem. A 7 (2019) 13928–13934.
[14] R. Gusmão, Z. Sofer, M. Pumera, Exfoliated layered manganese trichalcogenide phosphite ($MnPX_3$, X= S, Se) as electrocatalytic van der Waals materials for hydrogen evolution, Adv. Funct. Mater. 29 (2019) 1805975.
[15] J. Wang, X. Li, B. Wei, R. Sun, W. Yu, H.Y. Hoh, H. Xu, J. Li, X. Ge, Z. Chen, Activating basal planes of $NiPS_3$ for hydrogen evolution by nonmetal heteroatom doping, Adv. Funct. Mater. 30 (2020) 1908708.
[16] J. Zhang, N. Zhou, M. Du, Y. Li, Y. Cui, X.a. Li, X. Zhu, W. Huang, Cobalt single-atom-decorated nickel thiophosphate nanosheets for overall water splitting, J. Mater. Chem. A 10 (2022) 296–303.
[17] F. Ullah, K. Ayub, T. Mahmood, High performance SACs for HER process using late first-row transition metals anchored on graphyne support: a DFT insight, Int. J. Hydrogen Energy 46 (2021) 37814–37823.
[18] C.-H. Ho, T.-Y. Hsu, L.C. Muhimmah, The band-edge excitons observed in few-layer $NiPS_3$, npj 2D Mater. Appl. 5 (2021) 8.
[19] G. Kresse, D. Joubert, From ultrasoft pseudopotentials to the projector augmented-wave method, Phys. Rev. B 59 (1999) 1758–1775.
[20] P.E. Blöchl, Projector augmented-wave method, Phys. Rev. B 50 (1994) 17953–17979.
[21] J.P. Perdew, K. Burke, M. Ernzerhof, Generalized gradient approximation made simple, Phys. Rev. Lett. 77 (1996) 3865–3868.
[22] G. Kresse, J. Furthmüller, Efficient iterative schemes for ab initio total-energy calculations using a plane-wave basis set, Phys. Rev. B 54 (1996) 11169–11186.
[23] F. Aryasetiawan, K. Karlsson, O. Jepsen, U. Schönberger, Calculations of Hubbard U from first-principles, Phys. Rev. B 74 (2006) 125106.
[24] S.L. Dudarev, G.A. Botton, S.Y. Savrasov, C.J. Humphreys, A.P. Sutton, Electron-energy-loss spectra and the structural stability of nickel oxide: an LSDA+U study, Phys. Rev. B 57 (1998) 1505.
[25] H.J. Monkhorst, J.D. Pack, Special points for Brillouin-zone integrations, Phys. Rev. B 13 (1976) 5188–5192.
[26] S. Grimme, J. Antony, S. Ehrlich, H. Krieg, A consistent and accurate ab initio parametrization of density functional dispersion correction (DFT-D) for the 94 elements H-Pu, J. Chem. Phys. 132 (2010) 154104.

[27] G. Henkelman, B.P. Uberuaga, H. Jónsson, A climbing image nudged elastic band method for finding saddle points and minimum energy paths, J. Chem. Phys. 113 (2000) 9901–9904.
[28] K. Alam, T. Das, S. Chakraborty, P. Sen, Finding the catalytically active sites on the layered tri-chalcogenide compounds $CoPS_3$ and $NiPS_3$ for hydrogen evolution reaction, Phys. Chem. Chem. Phys. 23 (2021) 23967–23977.
[29] H. Lu, W. Wang, Y. Liu, L. Chen, Q. Xie, H. Yin, G. Cheng, L. He, Exfoliation, lattice vibration and air stability characterization of antiferromagnetic van der Waals $NiPS_3$ nanosheets, Appl. Surf. Sci. 504 (2020) 144405.
[30] J.K. Nørskov, T. Bligaard, A. Logadottir, J.R. Kitchin, J.G. Chen, S. Pandelov, U. Stimming, Trends in the exchange current for hydrogen evolution, J. Electrochem. Soc. 152 (2005) J23–J26.
[31] R.E. Mapasha, E. Igumbor, N. Chetty, A hybrid density functional study of silicon and phosphorus doped hexagonal boron nitride monolayer, J. Phys. Conf. Ser. 759 (2016) 012042.
[32] Y. Tong, P. Chen, L. Chen, X. Cui, Dual vacancies confined in nickel phosphosulfide nanosheets enabling robust overall water splitting, ChemSusChem 14 (2021) 2576–2584.
[33] A.A. El−Barbary, R.H. Telling, C.P. Ewels, M.I. Heggie, P.R. Briddon, Structure and energetics of the vacancy in graphite, Phys. Rev. B 68 (2003) 144107.
[34] D. Le, T.B. Rawal, T.S. Rahman, Single-layer MoS_2 with sulfur vacancies: structure and catalytic application, J. Phys. Chem. C 118 (2014) 5346–5351.
[35] X. Wang, Y. Zheng, W. Sheng, Z.J. Xu, M. Jaroniec, S.-Z. Qiao, Strategies for design of electrocatalysts for hydrogen evolution under alkaline conditions, Mater. Today 36 (2020) 125–138.
[36] Y. Li, Y. Guo, S. Yang, Q. Li, S. Chen, B. Lu, H. Zou, X. Liu, X. Tong, H. Yang, Mesoporous RhRu nanosponges with enhanced water dissociation toward efficient alkaline hydrogen evolution, ACS Appl. Mater. Interfaces 13 (2021) 5052–5060.
[37] G. Li, D. Zhang, Y. Yu, S. Huang, W. Yang, L. Cao, Activating MoS_2 for pH-universal hydrogen evolution catalysis, J. Am. Chem. Soc. 139 (2017) 16194–16200.
[38] G. Li, D. Zhang, Q. Qiao, Y. Yu, D. Peterson, A. Zafar, R. Kumar, S. Curtarolo, F. Hunte, S. Shannon, Y. Zhu, W. Yang, L. Cao, All the catalytic active sites of MoS_2 for hydrogen evolution, J. Am. Chem. Soc. 138 (2016) 16632–16638.
[39] Y. Ouyang, C. Ling, Q. Chen, Z. Wang, L. Shi, J. Wang, Activating inert basal planes of MoS_2 for hydrogen evolution reaction through the formation of different intrinsic defects, Chem. Mater. 28 (2016) 4390–4396.
[40] D. Liu, H. Ai, M. Chen, P. Zhou, B. Li, D. Liu, X. Du, K.H. Lo, K.W. Ng, S.P. Wang, Multi-phase heterostructure of CoNiP/Co_xP for enhanced hydrogen evolution under alkaline and seawater conditions by promoting H_2O dissociation, Small 17 (2021) 2007557.
[41] J. Wang, Z. Zhang, H. Song, B. Zhang, J. Liu, X. Shai, L. Miao, Water dissociation kinetic-oriented design of nickel sulfides via tailored dual sites for efficient alkaline hydrogen evolution, Adv. Funct. Mater. 31 (2021) 2008578.
[42] J. Zhang, T. Wang, P. Liu, S. Liu, R. Dong, X. Zhuang, M. Chen, X. Feng, Engineering water dissociation sites in MoS_2 nanosheets for accelerated electrocatalytic hydrogen production, Energy Environ. Sci. 9 (2016) 2789–2793.
[43] A. Roldan, N.H. de Leeuw, Catalytic water dissociation by greigite Fe_3S_4 surfaces: density functional theory study, Proc. Math. Phys. Eng. Sci. 472 (2016) 20160080.
[44] L. Zhang, Y. Zheng, J. Wang, Y. Geng, B. Zhang, J. He, J. Xue, T. Frauenheim, M. Li, Ni/Mo bimetallic-oxide-derived heterointerface-rich sulfide nanosheets with Co-doping for efficient alkaline hydrogen evolution by boosting Volmer reaction, Small 17 (2021) 2006730.
[45] C. Li, H. Gao, W. Wan, T. Mueller, Mechanisms for hydrogen evolution on transition metal phosphide catalysts and a comparison to Pt (111), Phys. Chem. Chem. Phys. 21 (2019) 24489–24498.
[46] Y. Chen, X. Zhang, J. Qin, R. Liu, Transition metal atom doped Ni_3S_2 as efficient bifunctional electrocatalysts for overall water splitting: design strategy from DFT studies, Mol. Catal. 516 (2021) 111955.
[47] A.B. Laursen, A.S. Varela, F. Dionigi, H. Fanchiu, C. Miller, O.L. Trinhammer, J. Rossmeisl, S. Dahl, Electrochemical hydrogen evolution: Sabatier's principle and the volcano plot, J. Chem. Educ. 89 (2012) 1595–1599.
[48] P. Wang, X. Zhang, J. Zhang, S. Wan, S. Guo, G. Lu, J. Yao, X. Huang, Precise tuning in platinum-nickel/nickel sulfide interface nanowires for synergistic hydrogen evolution catalysis, Nat. Commun. 8 (2017) 14580.
[49] Z. Ma, F. Wang, M. Dou, Q. Yao, F. Wu, E. Kan, Boosting the high-capacity with multi-active centers: a first-principles investigation of $NiPS_3$ monolayer as an anode material, Appl. Surf. Sci. 495 (2019) 143534.
[50] R.N. Jenjeti, R. Kumar, M.P. Austeria, S. Sampath, Field effect transistor based on layered $NiPS_3$, Sci. Rep. 8 (2018) 8586.
[51] P.J.S. Foot, J. Suradi, P.A. Lee, Optical and electronic properties of the layered semiconductors $NiPS_3$ and $FePS_3$, Mater. Res. Bull. 15 (1980) 189–193.
[52] Z. Wu, S. Xu, Y. Zhou, Q. Guo, Y. Dedkov, E. Voloshina, Adsorption of water molecules on pristine and defective $NiPX_3$ (X: S, Se) monolayers, Adv. Theory Simul. 4 (2021) 2100182.
[53] L. Guo, R. Li, J. Jiang, X. Fan, J.-J. Zou, W. Mi, Role of spin-resolved anti-bonding states filling for enhanced HER performance in 3d transition metals doped monolayer WSe_2, Appl. Surf. Sci. 599 (2022) 153979.
[54] F. Nie, Z. Li, X. Dai, X. Yin, Y. Gan, Z. Yang, B. Wu, Z. Ren, Y. Cao, W. Song, Interfacial electronic modulation on heterostructured NiSe@ CoFe LDH nanoarrays for enhancing oxygen evolution reaction and water splitting by facilitating the deprotonation of OH to O, Chem. Eng. J. 431 (2022) 134080.
[55] Q. Kong, X. An, L. Huang, X. Wang, W. Feng, S. Qiu, Q. Wang, C. Sun, A DFT study of $Ti_3C_2O_2$ MXenes quantum dots supported on single layer graphene: electronic structure an hydrogen evolution performance, Front. Phys. 16 (2021) 53506.